Journal of
Materials Chemistry A

PAPER

View Article Online
View Journal | View Issue

Cite this: *J. Mater. Chem. A*, 2017, **5**, 5791

Phase pure Sn_4P_3 nanotops by solution-liquid-solid growth for anode application in sodium ion batteries†

Danni Lan,[a] Wenhui Wang,[a] Liang Shi,[b] Yuan Huang,[a] Liangbin Hu[a] and Quan Li*[a]

Received 12th December 2016
Accepted 17th February 2017

DOI: 10.1039/c6ta10685d

rsc.li/materials-a

Sn_4P_3 is a promising anode material for sodium ion batteries due to its high capacity and suitable redox potentials relative to Na/Na^+. In Sn_4P_3 obtained by conventional fabrication methods, its large size (when obtained by ball milling) or the phosphorus (P) impurity left in the sample (when obtained by solvothermal treatment) is detrimental to the anode performance. In the present work, a facile solution chemistry method was developed to grow phase pure Sn_4P_3 nanotops with controllable size. Using trioctylphosphine (TOP) as the P source, the present method avoids the usage of flammable yellow P and the shelf-stable red P, the residue of which is difficult to remove after the reaction. The experimental results suggest solution-liquid-solid as the mechanism guiding the Sn_4P_3 growth. The Sn precursor plays an important role in determining the size and the morphology of the final Sn_4P_3 product. Such Sn_4P_3 nanotops show good electrochemical performance when employed as the anode for sodium ion batteries, giving an initial capacity of 719.8 mA h g^{-1} at a current density of 50 mA g^{-1}, an initial coulombic efficiency of about 72.7%, and reasonably good cyclability.

Introduction

Sodium ion batteries (SIBs) operating at ambient temperature have been considered as a promising alternative to lithium ion batteries due to Na abundance on earth and thus its low cost when employed for large storage applications.[1–4] Unlike Li-ion batteries, the anode development of SIBs remains challenging. Recently, intermetallic Sn_4P_3 has been proposed as a promising anode material for SIBs owing to its high theoretical volumetric capacity of about 1292 A h L^{-1},[5] high gravimetric capacity of 1132 mA h g^{-1} and reasonable redox potentials (~0.3 V for Na–Sn alloying and ~0.65 V for the Na–P compound *vs.* Na/Na^+, respectively).[6–8] Compared to individual tin (Sn) or phosphorus (P) based anodes, the Sn in the Sn_4P_3 acts as a conductive network for P, while the presence of P may reduce the Sn segregation to a certain extent during cycling.

High energy ball milling (HEBM) and solvothermal (ST) methods are two major fabrication methods to obtain Sn_4P_3.[9–14] The ball milling method employs Sn and red P powders as the starting materials and the resulting Sn_4P_3 alloys are usually of irregular shape and micron size. A relatively stable capacity of ~400–500 mA h g^{-1} at a current density of 100 mA h g^{-1} has been reported for the ball milled Sn_4P_3 with different carbon additives.[11,14] The relatively large size of the particles is expected to be detrimental to the electrochemical performance of the Sn_4P_3 based anode due to the rather slow kinetics of Na ion diffusion. Seeking possible control over the size and morphology of the Sn–P alloy, a solvothermal method has been developed by using red or yellow P and tin salts as source materials. Indeed, a small size (several to hundreds of nanometers) of Sn_4P_3 can be achieved. The solution chemistry based method also allows the modification of the Sn_4P_3 nanoparticles, for example, forming composites with various types of carbonaceous materials. These Sn_4P_3/C composites show a high capacity of ~600–800 mA h g^{-1} at a current density of 100 mA h g^{-1}.[7,15] However, the solvothermal Sn_4P_3 shows a rather low initial coulombic efficiency, likely due to the high values of irreversible capacity at the solid electrolyte interface and/or the presence of unreacted P source materials. On the other hand, it usually took several to tens of hours to obtain the Sn_4P_3 materials using either ball milling or solvothermal methods.

In the present work, we have developed a fast and facile solution chemistry method to fabricate phase pure Sn_4P_3 nanoparticles, which show a nanotop morphology with an average size of ~200 nm. Step by step compositional/structural analyses of the material at each growth stage suggest solution-liquid-solid (SLS) as the mechanism in guiding the Sn_4P_3 nanotop growth, and also disclose the critical role of the tin precursor in determining the size and morphology of the resulting Sn_4P_3. When employed as

---

[a] Department of Physics, The Chinese University of Hong Kong, Shatin, New Territory, Hong Kong, China. E-mail: liquan@phy.cuhk.edu.hk

[b] Department of Chemistry, University of Science and Technology of China, Hefei 230026, P. R. China

† Electronic supplementary information (ESI) available: Raman spectrum of the Sn_4P_3 nanotops, SEM-EDX mapping of the SnO balls, *ex situ* XRD patterns of Sn_4P_3 nanotop electrodes at different stages, voltage–capacity curves of MWCNTs at 100 mA g^{-1}, and EIS of the Sn_4P_3 nanotops with carbon layers on the surface and ball milled Sn_4P_3 without carbon layers. See DOI: 10.1039/c6ta10685d

the anode material for SIB, the as-synthesized Sn_4P_3 nanotops demonstrated a high specific capacity of 719.8 mA h g^{-1} at 50 mA g^{-1} and reasonable cycling stability. The present fabrication method can be generally applied to developing phase pure Sn based alloys with control over their size and morphology, which are important material parameters in determining their electrochemical properties for battery applications and beyond.

Experimental section

Materials preparation and characterization

All the reactions were carried out in an atmosphere of high purity nitrogen. As a general growth protocol, mixed reactants were first degassed at 120 °C for 0.5 h using a heating mantle in a flask under stirring with a reflux condenser. The mixtures were then aged, yielding a black solution. After cooling down to room temperature, the samples were washed and centrifuged with hexane four times. The final products were vacuum-dried. The special synthesis parameters are summarized below (Table 1).

The morphological and compositional analyses were carried out using a scanning electron microscope (SEM, JSM-7800F, JEOL). Transmission electron microscopy (TEM) based techniques were carried out using a Tecnai F20 ST (FEI) microscope operating at 200 kV. The crystallinity and phases of the samples were examined by X-ray diffraction (XRD, SmartLab, Rigaku) with a Cu-Kα radiation source ($d = 0.1541$ nm). Raman analysis was performed using a Micro Raman spectrometer (RM-1000, Renishaw Co., Ltd.) with a 10 mW helium neon laser at 514 nm. The electrodes that were cycled at a current density of 200 mA g^{-1} for *ex situ* XRD were disassembled in an inert-gas-filled glovebox, and the samples were sealed with polyimide tape (KAPTON, 2 mil thickness) before being transferred to the X-ray diffractometer.

Assembly of a 2032 coin-type half-cell with Na as the anode

The electrodes were prepared by spreading a slurry of 70 wt% active materials, 20 wt% multi-walled carbon nanotubes (MWCNTs) and 10 wt% sodium carboxymethylcellulose (CMC) binder on a copper foil substrate to form a thin film. The mass loading of the active materials within the film was about ~1 mg cm^{-2}. The MWCNT electrodes were assembled in the same way but only with 90 wt% MWCNT and 10 wt% CMC binder. A mixture of 1 M $NaClO_4$ in propylene carbonate (PC)/fluoroethylene carbonate (FEC) (95 : 5, by vol) was used as the electrolyte. Cyclic voltammetry (CV) and electrochemical impedance spectroscopy (EIS) measurements were performed on a CHI660c electrochemical workstation (ChenHua instrument Co., China). The galvanostatic charge/discharge test was conducted on a LAND CT2001A battery test system.

Table 1 Detailed information on the synthesis parameters for different samples[a]

	Parameters		
Samples	Reactants	Aging time	Aging temperature
SnO	10 mmol $Sn(acac)_2$ 40 mL TOP	1 h	300 °C
SnO & Sn	10 mmol $Sn(acac)_2$ 40 mL TOP	0.5 h	350 °C
Sn	10 mmol $Sn(acac)_2$ 40 mL TOP	1 h	350 °C
Sn/Sn_4P_3	2 mmol (0.23742 g) $Sn_{(pre)}$ 40 mL TOP	<1 h	350 °C
Sn_4P_3	2 mmol (0.23742 g) $Sn_{(pre)}$ 40 mL TOP	1 h	350 °C

[a] $Sn(acac)_2$: tin(II) acetylacetonate; TOP: trioctylphosphine; $Sn_{(pre)}$: as-prepared Sn precursors.

Results and discussion

Fig. 1a shows the X-ray diffraction (XRD) of the as-prepared Sn_4P_3 sample. All peaks can be indexed to the rhombohedral Sn_4P_3 (JCPDS # 73-1820). The morphology of the Sn_4P_3 sample is disclosed by scanning electron microscopy (SEM) (Fig. 1b). The Sn_4P_3 samples have a top-like morphology with faceted surfaces, and their sizes are in the range of 100–500 nm, with an average of 200 nm. The atomic ratio of Sn/P in the Sn_4P_3 nanotops is determined to be ~1.35 from energy-dispersive X-ray spectroscopy (EDS) (Fig. 1c), which is consistent with that of the stoichiometric Sn_4P_3 (1.33). The detailed microstructure of the Sn_4P_3 nanotops is investigated using transmission electron microscopy (TEM). Fig. 1d shows a low magnification TEM image of one Sn_4P_3 nanotop, in which a lighter contrast can be observed in the surface region of the nanotop. A corresponding C map (taken at the C K edge by using an electron energy loss spectrometer (EELS)) is taken from the same nanotop (Fig. 1e), revealing the presence of a thin carbon layer (of ~5 nm) on the surface of the nanotop. Raman spectroscopy has then been employed to characterize the carbon layers (ESI, Fig. S1†). Two peaks at 1344.4 and 1581.4 cm^{-1} are observed, which are attributed to the D (disordered) band and the G (graphite) band of carbon, respectively. The ratio of the integrated intensity between I_D and I_G bands is 3.58, indicating a low graphitization degree of the carbon layers. The formation of the surface carbon layer on Sn_4P_3 nanotops resulted from organic solvent capping and the adsorption of the organic solvent by the product during the reaction. A similar carbon shell has also been found in other chemical syntheses using TOP as the solvent.[16–18] Fig. 1f is a high resolution image taken at the interface between the crystalline Sn_4P_3 and the C surface layer. Lattice fringes can be seen in the Sn_4P_3 region, while the surface C appears to be amorphous. Fig. 1f shows the selected-area electron diffraction (SAED) pattern taken from a single Sn_4P_3 nanotop, suggesting its single crystalline nature.

The synthesis of the Sn_4P_3 nanotops consists of a few steps. First, SnO is synthesized from the thermal decomposition of tin(II) acetylacetonate ($Sn(acac)_2$) in TOP solvent. The XRD taken from the product suggests the formation of crystalline SnO of tetragonal structure (black line in Fig. 2). The as-formed SnO appears as large clusters with an average size of ~15 μm, (first column in Fig. 3). The chemical composition of such particles is revealed by EDS mapping when both Sn and O are present (ESI,

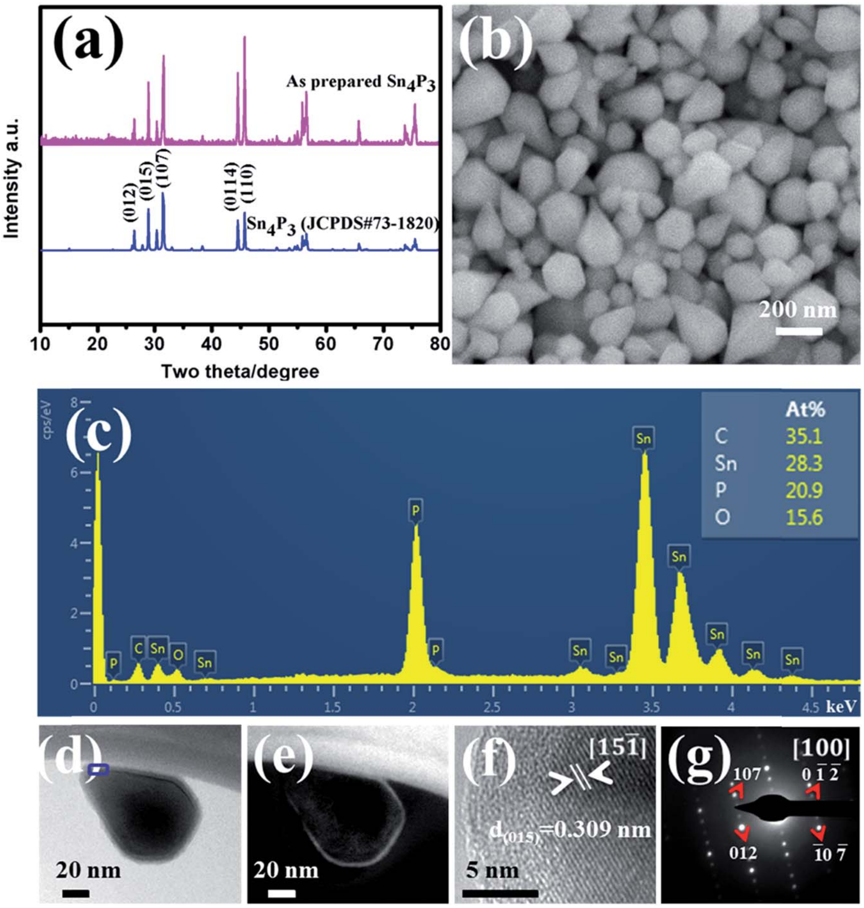

Fig. 1 (a) XRD of the Sn_4P_3 nanotops, (b) SEM image of the Sn_4P_3 nanotops, (c) EDS map taken from the Sn_4P_3 nanotops, (d) single Sn_4P_3 nanotop showing light contrast in its surface region, (e) carbon EELS map taken at the C K edge from the same Sn_4P_3 nanotop, (f) high resolution TEM image taken from the surface region of the nanotop, and (g) SAED taken from one Sn_4P_3 nanotop.

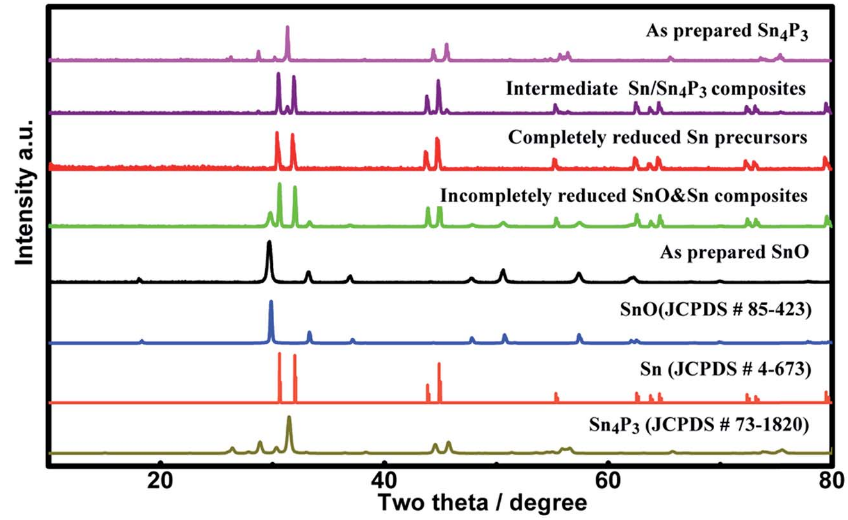

Fig. 2 XRD spectra of the products taken at different steps of Sn_4P_3 nanotop synthesis. Step 1: formation of SnO (black); Step 2: incomplete reduction of SnO to Sn (green); Step 3: complete reduction of SnO to Sn (red); Step 4: incomplete phosphorization of Sn (purple); and Step 5: formation of Sn_4P_3 (pink).

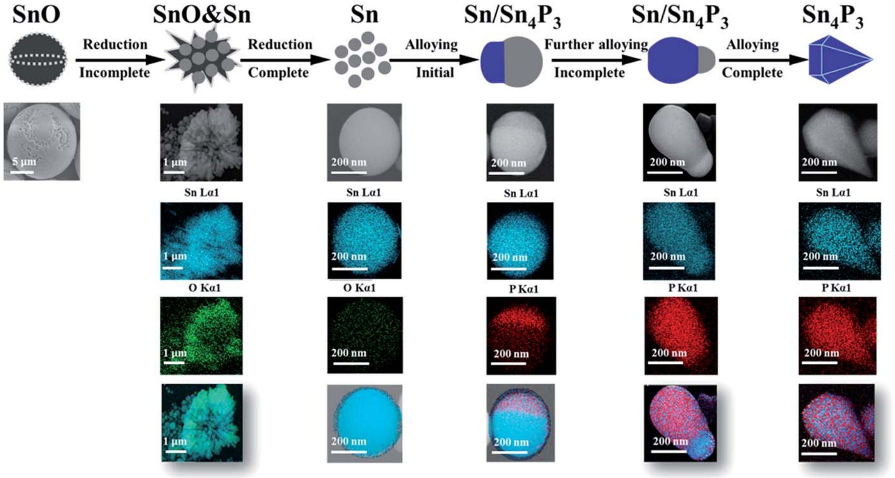

Fig. 3 Illustration of the growth process of Sn$_4$P$_3$ nanotops, supported by the corresponding SEM-EDS maps taken at different stages of growth.

Fig. S2†). The reduction of SnO clusters (with TOP as the reducing agent) in the second step leads to changes in the morphology of the product. The co-existence of SnO and Sn in such a sample is suggested by the XRD (green line in Fig. 2), revealing the incomplete reduction of SnO. The corresponding EDS maps disclose the formation of particles of much smaller size and smooth surface in the remaining architectures of SnO (Fig. 3). Further reduction of SnO–Sn composite clusters in the third step results in a completely reduced Sn crystal of spherical morphology. The XRD of such a product shows only a single Sn phase without any signals from the SnO (red line in Fig. 2). The corresponding EDS maps also confirm the main composition as Sn with a trace amount of O, which is inevitable due to surface oxidation. Using the Sn nanoparticles as the precursors and by re-adding the TOP solvent, alloying between Sn and P takes place. A sample taken from the intermediate stage of such a reaction shows XRD peaks that can be indexed to Sn and Sn$_4$P$_3$ (purple line in Fig. 2). The existence of intermediate stages is also supported by the EDS maps taken from the corresponding samples as shown in Fig. 3, in which one can observe the obvious interface between the Sn and the newly formed Sn–P alloy phase. With the alloying process proceeding, the size of the Sn in the particle keeps shrinking, while that of the Sn$_4$P$_3$ grows, until Sn is completely consumed and a final product with the uniform spatial distribution of Sn and P is obtained. The composition of the final product is Sn$_4$P$_3$, as suggested by the XRD taken from such a sample (pink line in Fig. 2).

The compositional and the morphological evolution of the Sn–P nanoparticles fabricated by phosphorization of Sn nanoparticles suggests solution-liquid-solid as the growth mechanism of the Sn$_4$P$_3$ nanoparticles. Fig. 4 presents the schematic illustration of such a mechanism. Tin is a metal of low melting point (231 °C) and would be easily melted to liquid droplets under the reaction temperature (350 °C). These liquid Sn catalysts can facilitate the cleavage of the P–C bond of the TOP and the decomposed P source would diffuse into the liquid droplets of Sn. Upon supersaturation, one of the stable phases in the Sn–P phase diagram with the lowest P content begins to solidify. A distinctive feature of the SLS growth is the presence of a catalyst (Sn in the present case) at one end of the nanoparticles during growth.[19–21] Usually a nanowire morphology is obtained *via* the SLS mechanism.[22–24] Nevertheless, one should note that in the present case Sn alloys with P and the supersaturated phase is Sn$_4$P$_3$ instead of P. This leads to the continuous consumption of Sn, providing a plausible explanation for the continuous shrinking of the Sn end and eventually the nanotop morphology of the Sn$_4$P$_3$. Consequently, this mechanism enables control over the size of the Sn$_4$P$_3$ nanotops, which is primarily determined by the size of the Sn nanoparticle precursors and also the extent of their aggregation during the phosphorization process.

The as-prepared Sn$_4$P$_3$ nanotops were used as the active material for the anode in the sodium ion battery. The electrochemical properties of the Sn$_4$P$_3$ nanotops were measured by assembling 2032-type coin cells (see methods). Fig. 5a shows

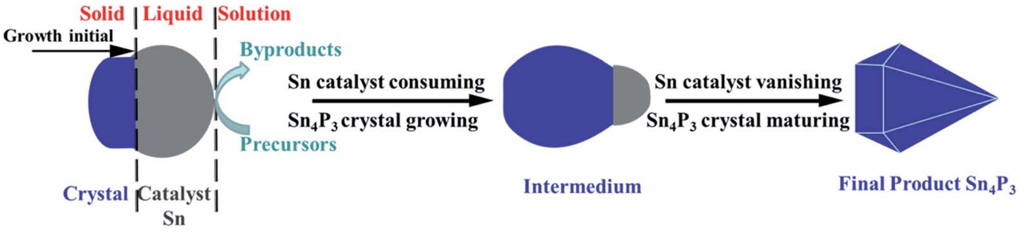

Fig. 4 Schematic illustration of the growth mechanism of Sn$_4$P$_3$.

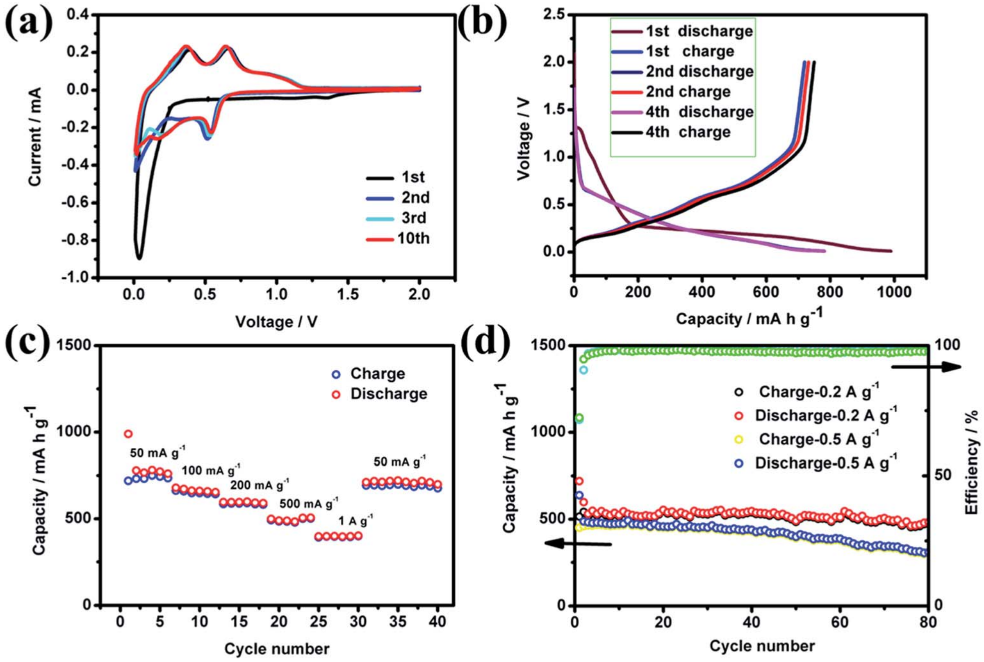

Fig. 5 Electrochemical performances of Sn_4P_3 nanotop anodes: (a) CV curves at a scan rate of 0.05 mV s^{-1} in the voltage range of 0.01–2.0 V; (b) voltage–capacity curves at 50 mA g^{-1}; (c) rate capability at different rates (increasing from 50 mA g^{-1} to 1 A g^{-1}); (d) cycling performances of Sn_4P_3 nanotops at 0.2 A g^{-1} and 0.5 A g^{-1}.

the CV plots taken at a scan rate of 0.05 mV s^{-1}. In the first cathodic cycle, a small peak appears at ~1.3 V (*vs.* Na^+/Na) mainly due to the formation of a solid electrolyte interphase (SEI). A shoulder follows at ~0.25 V, which is consistent with the sodiation of Sn_4P_3 ($Sn_4P_3 + Na^+ \rightarrow Na_{15}Sn_4 + Na_3P$).[11] In the first anodic cycle, two peaks appear at ~0.36 and ~0.65 V, respectively. The ~0.36 V peak is associated with the desodiation of $Na_{15}Sn_4$ ($Na_{15}Sn_4 \rightarrow Sn + Na_xSn_y + Na^+$), and the other one at 0.65 V can be assigned to the desodiation of Na_3P ($Na_3P \rightarrow P + Na^+$) along with the further desodiation of Na–Sn alloys ($Na_xSn_y \rightarrow Sn + Na^+$)[7,11] and re-alloying of Sn and P back to Sn_4P_3.[6] It is important to note that the re-alloying process is not complete, as *ex situ* XRD results reveal the co-existence of Sn and Sn_4P_3 after the first charge/discharge cycle (ESI, Fig. S3†). The partial reversibility (in regaining the Sn_4P_3 phase) may contribute to the deterioration of the anode performance during cycling. In the subsequent cathodic cycles, peaks at 0.54 V and 0.18 V show up apparently; the ~0.54 V peak can be ascribed to the first step of sodiation ($Sn_4P_3 + Na^+ \rightarrow Sn + Na_xSn_y + Na_3P$), and another peak at ~0.18 V is linked to the further sodiation reaction of Na–Sn alloys ($Na_xSn_y + Na^+ \rightarrow Na_{15}Sn_4$).[7,11] The reaction chemistry remains similar in the following anodic cycles.

Fig. 5b shows the galvanostatic discharge/charge plots of the Sn_4P_3 nanotop electrode in the voltage window of 0.01–2.00 V. The first discharge/charge process delivers a specific capacity of 989 and 719.8 mA h g^{-1}, with a high initial coulombic efficiency of 72.7%. In the fourth cycle, the charge capacity increases to 749.8 mA h g^{-1}, indicating a slight activation process. Good rate capabilities are suggested by the rate performance data of the Sn_4P_3 nanotops as shown in Fig. 5c. The capacities are measured to be 749, 659, 591, 501, and 399 mA h g^{-1} at 50, 100, 200, 500, and 1000 mA g^{-1}. Reasonable cycling performance of these Sn_4P_3 nanotops is obtained (Fig. 5d). At a current density of 0.2 A g^{-1}, 92% capacity of Sn_4P_3 nanotops is retained after 80 cycles. At a higher current density of 0.5 A g^{-1}, the capacity can remain at 400 mA h g^{-1} (82% capacity retention) after 50 cycles and then gradually drops to 67% of the initial capacity. During cycling, the peaks of Sn_4P_3 gradually vanish and the peak intensity of Sn increases (ESI, Fig. S3†), indicating a segregation process of Sn, which could be one of the reasons for the deterioration of the anode performance during cycling. The conductive additives (multi-walled carbon nanotubes (MWCNTs) in the present case) themselves have little contribution to the reversible capacity (ESI, Fig. S4†). Although there is a thin surface carbon layer on the as-grown Sn_4P_3, the existence of such a layer has little effect on the overall electrical conductivity of the electrode, and thus does not affect the electrochemical performance of the Sn_4P_3 electrode in any significant manner (ESI, Fig. S5†).

Fig. 6 summarizes the main results of Sn–P based anodes for SIBs in the literature. The performance of the Sn_4P_3 nanotops in the present work is among the best. Compared to the ball-milled Sn_4P_3 particles that are usually in the range of micrometers, the SLS growth mechanism enables the control of the size of the Sn_4P_3 nanotops (which is mainly determined by the size and aggregation of the Sn precursors). The smaller size of the Sn_4P_3 nanotops then contributes to the shortening of the charge carrier diffusion length and/or alleviating the strain during charging/discharging cycles, and eventually leads to the improved rate performance of the Sn_4P_3 nanotops (compared to

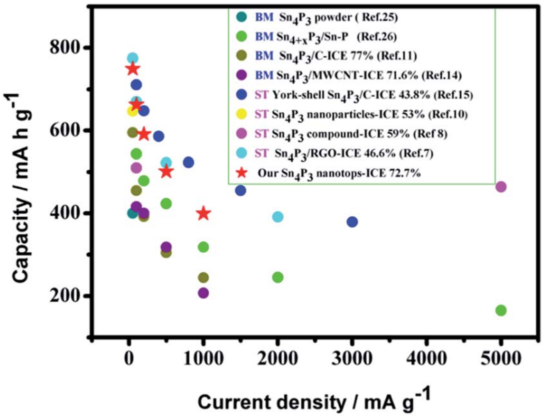

Fig. 6 Comparison of the performance of the Sn–P based anodes for SIBs (BM means ball milling; ST means solvothermal; ICE means initial coulombic efficiency). All the capacities are calculated based on the as-prepared whole active materials, including the carbonaceous compound.

the ball-milled Sn–P materials). On the other hand, although the size of Sn–P materials grown from solution chemistry is usually small, conventional approaches usually involve P as the reactant, which is likely to remain in the final products (difficult to remove from the Sn_4P_3 products).[8] The absence of P in the present samples provides an explanation for the relatively high coulombic efficiency of the Sn_4P_3 nanotops anodes.

Conclusion

In conclusion, Sn_4P_3 nanotops with an average size of 200 nm have been successfully synthesized by carefully designing the solution chemistry using $Sn(acac)_2$ as the Sn source and TOP as the P source. Structural and compositional analyses of the product at each synthetic step disclose SLS as the mechanism guiding the growth of the nanotops. Such a mechanism provides us a facile approach to control the size and the morphology of the Sn_4P_3. Moreover, the employment of TOP as the P source excludes the presence of residual P, which is common and difficult to remove in conventional solvothermal growth. The small size and the pure phase of Sn_4P_3 nanotops result in a high capacity of 719.8 mA h g^{-1} and a good cyclability (92% capacity retention over 80 cycles at a current density of 0.2 A g^{-1}). The Sn_4P_3 nanotop anode also shows a reasonable initial coulombic efficiency of 72.7% (usually less than 60% in solvothermal samples).

Conflict of interest

The authors declare no competing financial interest.

Acknowledgements

This work is supported by the RGC/GRF under project No. 14316716.

References

1 N. Yabuuchi, K. Kubota, M. Dahbi and S. Komaba, *Chem. Rev.*, 2014, **114**, 11636–11682.
2 L. P. Wang, L. Yu, X. Wang, M. Srinivasan and Z. J. Xu, *J. Mater. Chem. A*, 2015, **3**, 9353–9378.
3 M. D. Slater, D. Kim, E. Lee and C. S. Johnson, *Adv. Funct. Mater.*, 2013, **23**, 947–958.
4 D. Kundu, E. Talaie, V. Duffort and L. F. Nazar, *Angew. Chem., Int. Ed. Engl.*, 2015, **54**, 3431–3448.
5 L. Zheng, R. A. Dunlap and M. N. Obrovac, *J. Electrochem. Soc.*, 2016, **163**, A1188–A1191.
6 Y. Kim, Y. Kim, A. Choi, S. Woo, D. Mok, N. S. Choi, Y. S. Jung, J. H. Ryu, S. M. Oh and K. T. Lee, *Adv. Mater.*, 2014, **26**, 4139–4144.
7 Q. Li, Z. Li, Z. Zhang, C. Li, J. Ma, C. Wang, X. Ge, S. Dong and L. Yin, *Adv. Energy Mater.*, 2016, 1600376, DOI: 10.1002/aenm.201600376.
8 H. S. Shin, K. N. Jung, Y. N. Jo, M. S. Park, H. Kim and J. W. Lee, *Sci. Rep.*, 2016, **6**, 26195.
9 K. A. Kovnir, Y. V. Kolen'ko, S. Ray, J. Li, T. Watanabe, M. Itoh, M. Yoshimura and A. V. Shevelkov, *J. Solid State Chem.*, 2006, **179**, 3756–3762.
10 S. Liu, H. Zhang, L. Xu, L. Ma and X. Chen, *J. Power Sources*, 2016, **304**, 346–353.
11 J. Qian, Y. Xiong, Y. Cao, X. Ai and H. Yang, *Nano Lett.*, 2014, **14**, 1865–1869.
12 J. Y. Jang, Y. Lee, Y. Kim, J. Lee, S.-M. Lee, K. T. Lee and N.-S. Choi, *J. Mater. Chem. A*, 2015, **3**, 8332–8338.
13 S. Liu, S. Li, M. Li, L. Yan and H. Li, *New J. chem.*, 2013, **37**, 827.
14 J. Mao, X. Fan, C. Luo and C. Wang, *ACS Appl. Mater. Interfaces*, 2016, **8**, 7147–7155.
15 J. Liu, P. Kopold, C. Wu, P. A. van Aken, J. Maier and Y. Yu, *Energy Environ. Sci.*, 2015, **8**, 3531–3538.
16 Y. Lu, J. P. Tu, J. Y. Xiang, X. L. Wang, J. Zhang, Y. J. Mai and S. X. Mao, *J. Phys. Chem. C*, 2011, **115**, 23760–23767.
17 D. Yang, J. Zhu, X. Rui, H. Tan, R. Cai, H. E. Hoster, D. Y. Yu, H. H. Hng and Q. Yan, *ACS Appl. Mater. Interfaces*, 2013, **5**, 1093–1099.
18 P. K. Khanna, K.-W. Jun, K. B. Hong, J.-O. Baeg and G. K. Mehrotra, *Mater. Chem. Phys.*, 2005, **92**, 54–58.
19 F. Wang, A. Dong and W. E. Buhro, *Chem. Rev.*, 2016, **116**, 10888–10933.
20 M. I. Bodnarchuk, K. V. Kravchyk, F. Krumeich, S. Wang and M. V. Kovalenko, *ACS Nano*, 2014, **8**, 2360–2368.
21 F. Wang, A. Dong, J. Sun, R. Tang, H. Yu and W. E. Buhro, *Inorg. Chem.*, 2006, **45**, 7511–7521.
22 M.-S. Kim and Y.-M. Sung, *Chem. Mater.*, 2013, **25**, 4156–4164.
23 Z. Li, L. Cheng, Q. Sun, Z. Zhu, M. J. Riley, M. Aljada, Z. Cheng, X. Wang, G. R. Hanson, S. Qiao, S. C. Smith and G. Q. Lu, *Angew. Chem., Int. Ed. Engl.*, 2010, **49**, 2777–2781.
24 J. Sun and W. E. Buhro, *Angew. Chem.*, 2008, **120**, 3259–3262.
25 H. Usui, T. Sakata, M. Shimizu and H. Sakaguchi, *Electrochemistry*, 2015, **83**, 810–812.
26 W. Li, S. L. Chou, J. Z. Wang, J. H. Kim, H. K. Liu and S. X. Dou, *Adv. Mater.*, 2014, **26**, 4037–4042.